Composites: Part A 92 (2017) 51–61

Contents lists available at ScienceDirect

Composites: Part A

journal homepage: www.elsevier.com/locate/compositesa

3D *in situ* observations of the compressibility and pore transport in Sheet Moulding Compounds during the early stages of compression moulding

D. Ferré Sentis [a,b,c,d], L. Orgéas [a,*], P.J.J. Dumont [c], S. Rolland du Roscoat [a], M. Sager [c], P. Latil [e]

[a] CNRS, Univ. Grenoble Alpes, 3SR Lab, F-38000 Grenoble, France
[b] Univ. Lyon, INSA-Lyon, CNRS UMR5259, LaMCoS, F-69621, France
[c] Plastic Omnium Auto Exterior, Sigmatech, F-01150 Sainte Julie, France
[d] CNRS, Univ. Grenoble Alpes, LGP2, F-38000 Grenoble, France
[e] Novitom, 1 Place Firmin Gautier, F-38000 Grenoble, France

ARTICLE INFO

Article history:
Received 16 July 2016
Received in revised form 27 October 2016
Accepted 29 October 2016
Available online 31 October 2016

Keywords:
A. Prepreg
B. Porosity
D. X-ray microtomography
E. Compression moulding

ABSTRACT

The properties of Sheet Moulding Compounds (SMCs) are altered by their porosity induced during the manufacturing or moulding of these prepregs. To characterise the pore scale mechanisms occurring during SMC flow, 3D synchrotron X-ray images were acquired during the compression of two uncured SMCs. For the high fibre content SMC (50 wt%), with a high porosity, pores mainly decreased in size and disappeared during SMC consolidation. These mechanisms were related to the elasticity of the fibrous networks and to the permeability of the porous phase, estimated using pore scale CFD simulation. For the standard fibre content SMC (29 wt%), with a lower porosity, the compressibility was limited and closed pores were transported towards the external surface of samples with non-affine motion, *i.e.*, faster than the SMC flow and with tortuous trajectories. Besides, pores coalesced and decreased in size during compression. The size decrease was mainly related to the dissolution of pore gases.

1. Introduction

Thanks to their excellent properties and their cost effectiveness, Sheet Moulding Compounds (SMCs) are thermoset prepregs that are broadly used in the aeronautical, automotive and electrical industries to manufacture body and structural parts. They are usually composed of a thermoset matrix (polyester, vinylester, epoxy) reinforced with 15 to 60 wt% of chopped fibres (glass or carbon fibre bundles, biosourced fibres) and are prepared in the form of 1–3 mm sheets [1]. The sheet processing consists of three steps: paste mixing, impregnation of the fibre network by the thermoset polymer paste, calendering and paste thickening. As for some other prepregs, SMCs exhibit a non-negligible amount of pores (≈1–20% after their fabrication [2–6]. In addition, during their forming phase, *i.e.*, compression moulding, initial pores can be transported, their size decreases and they can disappear [4,5,7–8]. Other pores can also nucleate or be introduced into the SMCs, *e.g.* by solvent boiling or squish flow phenomena at the flow front, respectively [5,9]. These intricate mechanisms are accompanied by the deformation of the fibrous reinforcement with complex volume variations. They can result in the appearence of pores which usually lower the physical and mechanical properties of moulded parts [10–12]. Among the challenges to overcome to optimise compression moulding of SMCs and the end-use properties of produced parts, understanding and modelling the aforementioned phenomena is a critical issue. To this end, various experimental studies were conducted to find how to reduce SMC porosity during compression moulding, *e.g.* by using vacuum assisted moulding, tuning the mould closing pressure or velocity and the mould temperature or by preheating SMCs before compression [5,12–14]. However, pore scale mechanisms are still not very well understood so that, to the authors' knowledge, there is no proper description and model of pore kinetics and kinematics during compression moulding of SMCs. Consequently, to date, the compression moulding stage is generally numerically simulated assuming that SMCs are incompressible [2,3,15–20], which is a strong *a priori* assumption when considering the SMC initial pore contents.

It is worth mentioning that pore kinetics and kinematics was extensively studied for other prepregs, see for examples [21–24] among the numerous studies. These studies provide interesting guidelines to understand and model pore mechanisms that occur in prepregs as well as observations of the pore morphology. However, most of the studied prepregs do not exhibit in-plane flow during their forming stage, whereas SMCs are usually subjected to substantial in-plane flow during compression moulding [1]. This

* Corresponding author.
E-mail address: Laurent.Orgeas@3sr-grenoble.fr (L. Orgéas).

http://dx.doi.org/10.1016/j.compositesa.2016.10.031
1359-835X/

probably yields other pore transport mechanisms. In addition, in most of the aforementioned studies, 3D quantitative analyses of the pore morphology and evolution, *e.g.* using X-ray microtomography [25], are scarce. Recently, Centea and Hubert [23] used this technique to analyse the evolution of pores in out-of-autoclave prepregs. Thanks to X-ray microtomography, consolidation mechanisms were better understood. However, as the considered prepregs exhibited continuous fibre bundles, the in-plane flow of the prepregs was limited, whereas this flowing mode can be important in SMCs as fibre bundles are discontinuous. In addition, samples were imaged *ex situ* so that the issue of the *in situ* evolution of pores was not tackled. This is now possible using synchrotron X-ray sources, which enable the acquisition of 3D images at very fast scanning times and to perform real-time 3D *in situ* observations of the structure of composites during their deformation [26,27].

Thus, the objective of this study was to complete these former experimental studies to better characterise the pore kinetics and kinematics during compression moulding of SMCs. For that purpose, we studied the compressibility, the evolution of the content and morphology of pores as well as their transport in two uncured SMC formulations having standard and high fibre contents, respectively. Hence, a compression rheometer was specially designed and mounted in the synchrotron X-ray microtomograph of the ID19 beamline (ESRF, Grenoble, France). Then, rheometry experiments were performed while scanning prepregs at different compression stages. This method also enabled 3D *in situ* images of the evolving mesostructures to be reconstructed. These original data were combined with macroscale strains measurements that were simultaneously recorded during the compression experiments to give a relevant analysis of the early stages of compression moulding of SMC.

2. Materials and methods

2.1. Materials

Two industrial formulations of SMC with two very different fibre contents were used and prepared by MCR – Plastic Omnium (Tournon-sur-Rhône, France). The first SMC formulation, which was denoted by the letter *S*, is typically used to produce lightweight automotive semi-structural parts. It consisted of a polyester-based paste reinforced with 29 wt% of flat glass fibre bundles with a 25-mm length, approximately 0.05 mm in height and 0.5 mm in width. The rheological behaviour of this formulation was similar to that reported for other SMCs in previous studies [28,29]. The second SMC formulation is used to produce structural parts. It was denoted by *H* in the following sections and consisted of a vinylester-based paste reinforced with 50 wt% of glass fibre bundles having similar dimensions than those of the *S* formulation. For compression tests, five cylindrical samples were cut out of both SMCs. These samples were made of two stacked sheets, leading to initial sample heights h_0 approximately equal to 4 and 6 mm for the *H* and *S* SMCs, respectively. The initial diameter D_0 of the samples were chosen to acquire 3D images with the best spatial resolution, *i.e.,* to extract relevant information on both the pore mesostructures and macroscale sample flow mechanisms. Thus, the diameter D_0 was set to 30 mm for the *H* samples and for one *S* sample (Table 1). The two other studied *S* samples had a lower initial diameter of 20 mm (Table 1) in order to analyse the onset of their in-plane flow at higher compressive strains. Further, it was observed that the sample macroscale surface and volume strains (next subsection) were very close to those measured during lubricated compression experiments (not shown here) using the same transparent rheometer as reported by Guiraud et al. [30] for samples with larger 55-mm diameter. In addition, it was also verified that the samples with 20-mm and 30-mm diameters exhibited similar pore content and morphology (Fig. 4(c)), in the initial state but also during compression: their typical size was sufficiently small with respect to the investigated sample diameters so that the results could be considered to be representative [31].

2.2. Compression tests with 3D in situ X-ray imaging

The compression experiments were designed to mimic what is observed in many flow situations during SMC compression moulding: out-of-plane consolidation and in-plane plug flow of the core of SMCs at moderate temperatures (≈40–100 °C), combined with intensive shear of hot (≈150 °C) paste-rich outer layers acting as low viscosity lubricants [8,9,32,33]. Thus, as a first step towards more realistic configurations, the SMC samples were subjected to lubricated simple compression loading at room temperature (25 °C) using a specially designed compression rheometer similar to that used in previous studies [34,35] but equipped with a load cell of higher capacity (2kN). The SMC samples were positioned on the lower moving compression platen (Fig. 1). The vertical motion of the lower platen was achieved using an electromechanical actuator and gearing (maximal translation velocity of 300 $\mu m\,s^{-1}$). The SMC samples were subjected to a very small pre-compression (0.017 MPa) to ensure the contact with the platens. After stress relaxation (≈3 min), the mechanical loading was applied from the actuator attached to the lower compression platen so that the compression experiments were performed at two constant velocities $\dot{h}$, *i.e.*, 5 and 50 $\mu m\,s^{-1}$, corresponding to two initial compressive strain rates $D_{33}^0 = \dot{h}/h_0$ of 0.001 and 0.01 s^{-1} along the direction $\mathbf{e}_3$. These strain rates correspond to those encountered by SMC during moulding of parts with a midplane that is not perpendicular to the principal compression direction (taking into account typical compression moulding velocities that range between 0.01 and 10 mm s^{-1}). From an industrial standpoint, these flow zones are considered to be critical since pores are more difficult to extract, even at high mould closing pressure. The propagation distance between the sample and the X-ray detector was set to 4 m, enabling 3D-image reconstruction (the so-called Paganin reconstruction mode) based on enhanced phase contrast [36]. The following acquisition parameters were also used: 1999 X-ray projections (beam energy of 45 keV) acquired with a 360° rotation of the micro-rheometer. Then, thanks to high speed PCO edge camera, a very short scanning time of 2 s for each 3D image was obtained. For the highest strain rate, only interrupted loading experiments were performed and 8 scans were taken. When a targeted sample height *h* was reached, the test was stopped (for 2 s), a scan was taken and the loading was continued until the next stage. For the experiments performed at the lowest strain rate, interrupted but also continuous scans were performed, and 6–9 scans were obtained. In the particular case of the S4 sample, 30 images were acquired without stopping the loading, enabling real-time *in situ* 3D observations. Three-dimensional images of the internal structure of the sample, with volumes of size $1698 \times 1698 \times 464$ voxels and with a voxel size of 23.5^3 μm^3 (Fig. 2(a) and (b)), were obtained using suitable reconstruction algorithms.

2.3. Image analysis and data post-treatment

Most of the image analysis was achieved using the softwares Fiji [37] and Matlab. Standard filtering operations (median and Gaussian filter) were used to obtain 3D grey scale images that enabled the macroscale strains of the compressed samples to be measured. The height *h* of each sample was precisely measured to estimate the Hencky compressive strain $\varepsilon_{33} = \ln(h/h_0)$ (Fig. 2(a)). In addition, we also estimated the mean area $\overline{A}$ of the sample in-plane

Table 1
Test number with their characteristics: type of SMC formulation, fibre content, initial diameter D_0, initial compressive strain rate D^0_{33}, and compression loading type (interrupted or continuous).

Test number	1	2	3	4	5
Sample type	*H*	*H*	*S*	*S*	*S*
Fibre content (wt%)	50	50	29	29	29
D_0 (mm)	30	30	30	20	20
D^0_{33} (s^{-1})	0.001	0.01	0.01	0.001	0.01
Loading type	Continuous	Interrupted	Interrupted	Continuous	Interrupted

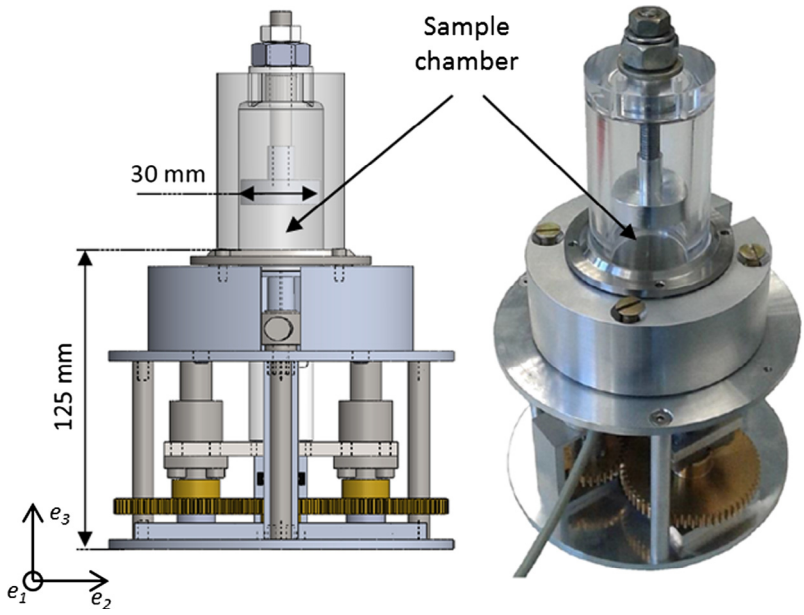

Fig. 1. Scheme and photographs of the compression rheometer installed in the synchrotron X-ray microtomograph of the ID19 beamline (ESRF, Grenoble, France). (For interpretation of the references to colour in this figure legend, the reader is referred to the web version of this article.)

surface, *i.e.*, the mean sample surface in the $(\mathbf{e}_1, \mathbf{e}_2)$ plane. For that purpose, the sample areas within a dozen of in-plane cross sections were estimated, $\overline{A}$ being their mean value. Notice that for each slice the SMC area was measured using the function "Wand" of Fiji. Filling operations were also used to remove pores. Then, the sample surface strain $\varepsilon_S = \ln(\overline{A}/\overline{A}_0)$ and the sample volumetric strain $\varepsilon_V = \varepsilon_S + \varepsilon_{33}$ were calculated. Other image analysis operations were performed using the binarised images. As shown in Fig. 2 (c)–(f), the good contrast between the pore phase and the solid phases of the sample (enhanced by the Paganin imaging reconstruction) enabled easy manual thresholding and measurements of several descriptors for the pore phase. These analyses were achieved in cylindrical or cubic Regions Of Interest (ROIa) and (ROIb), respectively, depending on the used algorithms, as shown in Fig. 2(b):

- The volume fraction of pores ϕ_p in the sample was calculated by counting the number of voxels of the pore phase and dividing it by the number of voxels of the ROIa.
- We also computed 2D mean porosity $\overline{\phi}_{p2D}$ maps along the plane $(\mathbf{e}_1, \mathbf{e}_2)$ of the sheets to observe qualitatively pore transport and pore size decrease during the sample compression, as illustrated in Fig. 3. Each pixel $p(i,j)$ of the 2D colormaps corresponded to a porosity defined as the porosity of the subvolume (thickness of N voxels) given by the set of voxels $v(i,j,k)$ of the corresponding initial 3D images ($k \in [1, N]$). The plugin "Pointpicker" of Fiji was also used to follow quantitatively the in-plane motion of the centre of mass in these images with respect to the centre of mass of the samples.
- The plugin "BoneJ" of Fiji [38] was used to perform connectivity analysis in the porous phase of ROIb. This plugin was used to detect closed pores in the images, *i.e.*, pores which were not connected with at least one edge of the ROIs. Then, the mean volume $\overline{V}_{cp}$ of the closed pores was calculated using the plugin "Particle Analyser" of Fiji. In addition, the volume fractions of closed ϕ_{cp} and open pores $\phi_{op} = \phi_p - \phi_{cp}$ in the samples were calculated.
- The anisotropy of the pore phase was estimated in ROIb by computing the mean chord lengths l_1, l_2, and l_3 of the pore phase along the $\mathbf{e}_1$, $\mathbf{e}_2$ and $\mathbf{e}_3$ directions, respectively [39]. Then, the anisotropy ratios $r_{12} = l_1/l_2$, $r_{13} = l_1/l_3$ and $r_{23} = l_2/l_3$ were calculated to quantify the mean shape of pores.

The motion of several selected closed pores i along the $(\mathbf{e}_1, \mathbf{e}_2)$ was also analysed in one of the S samples. For that purpose, the 2D positions $\tilde{\mathbf{x}}^{exp}_{G_i}$ of their centres of mass G_i were tracked from Fig. 3. Then, these positions were compared with the positions $\tilde{\mathbf{x}}^{aff}_{G_i}$ that these pores would have followed assuming an affine motion with the SMC:

$$\tilde{\mathbf{x}}^{aff}_{G_i} = \tilde{\mathbf{x}}^{exp0}_{G_i} + \int_0^t \frac{\dot{\varepsilon}_s}{2}(\mathbf{e}_1 \otimes \mathbf{e}_1 + \mathbf{e}_2 \otimes \mathbf{e}_2)\mathrm{d}t, \quad (1)$$

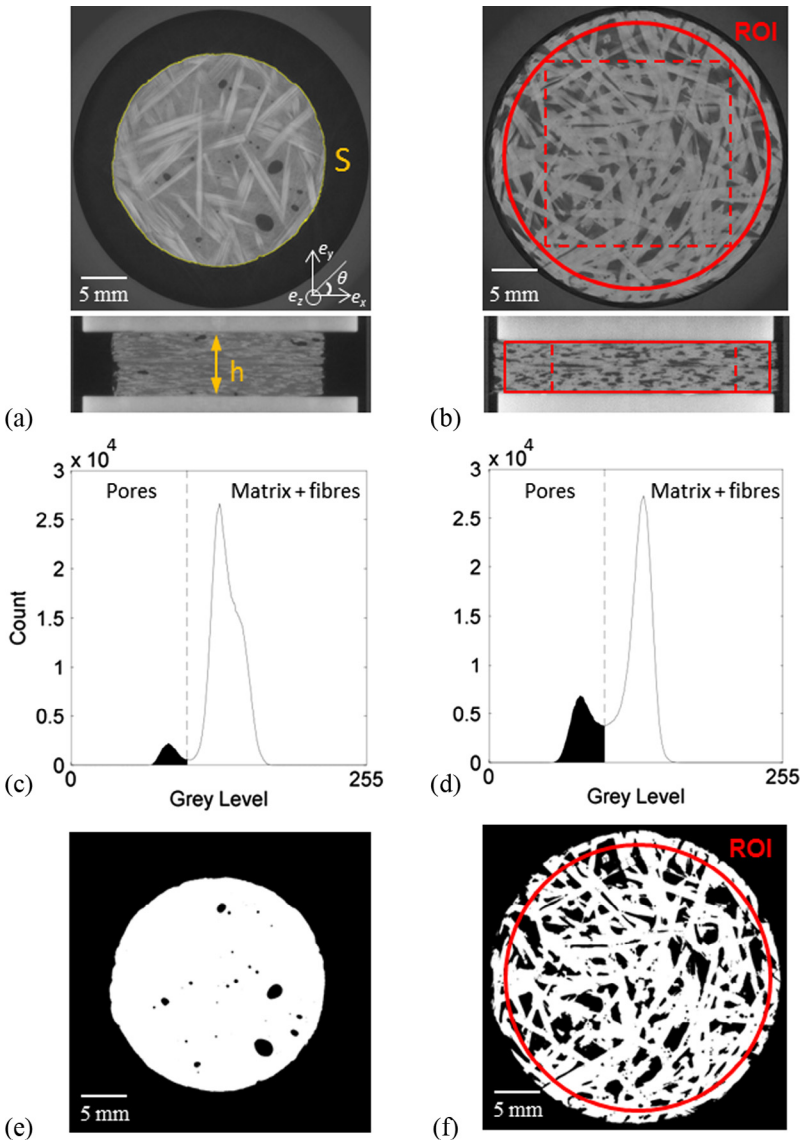

Fig. 2. Initial grey scale slices of one *S* (a) and one *H* (b) samples. In (b), ROIa and ROIb are represented with dotted and continuous lines, respectively. (c, d) Histograms of the images (ROIb) of the upper slices shown in (a, b). (e, f) Examples of thresholded slices. (For interpretation of the references to colour in this figure legend, the reader is referred to the web version of this article.)

where $\tilde{\mathbf{x}}_{G_i}^{exp0}$ were the initial in-plane positions of the considered pores. For comparison, the deviations $\Delta x_{G_i} = \tilde{\mathbf{x}}_{G_i}^{exp} - \tilde{\mathbf{x}}_{G_i}^{aff}/h_0$ were also estimated.

2.4. Permeability estimation

To analyse and discuss the experimental results, the permeability tensor **K** of the porous media constituted by the fibre bundles and the paste matrix was calculated (Section 3) using (i) the 3D binarised images (ROIb) obtained during the compression of the two SMC formulations, (ii) the theoretical framework of the homogenisation method with multiple asymptotic expansions [40], (iii) and pore scale fluid flow numerical simulation using the 3D images [41,42]. Practically, the Finite Volume software GeoDict was used to compute the permeability tensor **K** by solving the Stokes localisation problem deduced from the homogenisation using 3D segmented images as calculation volumes. Details about this procedure are reported by Chalencon et al. [42].

3. Results

3.1. Initial mesostructures

The vertical and horizontal slices shown in Fig. 2, the two first 2D maps shown in Fig. 3 and the 3D views shown in Fig. 4 (a) and (b) show that both SMC formulations exhibited pores before compression.

For the *S* formulation, the initial average porosity ϕ_{p0} was approximately 0.025 (Fig. 5(a)), with large variations between samples (from 0.015 to 0.055). These values were close to those previously reported for this type of SMCs [4,5]. In addition, this formulation exhibited a significant amount of closed and isolated pores since the initial closed pore content ϕ_{cp0} was approximately 0.015 (Fig. 6(a)). The pores that were initially closed had rounded and ellipsoidal shapes with a moderate transverse isotropy and larger in-plane dimensions (Fig. 7(a)). It was verified that the transverse isotropy measured for each sample, made of several layers, was identical to that given when analysing only one SMC layer. The arrow in Fig. 4(a) and (b) shows that open pores were very flat.

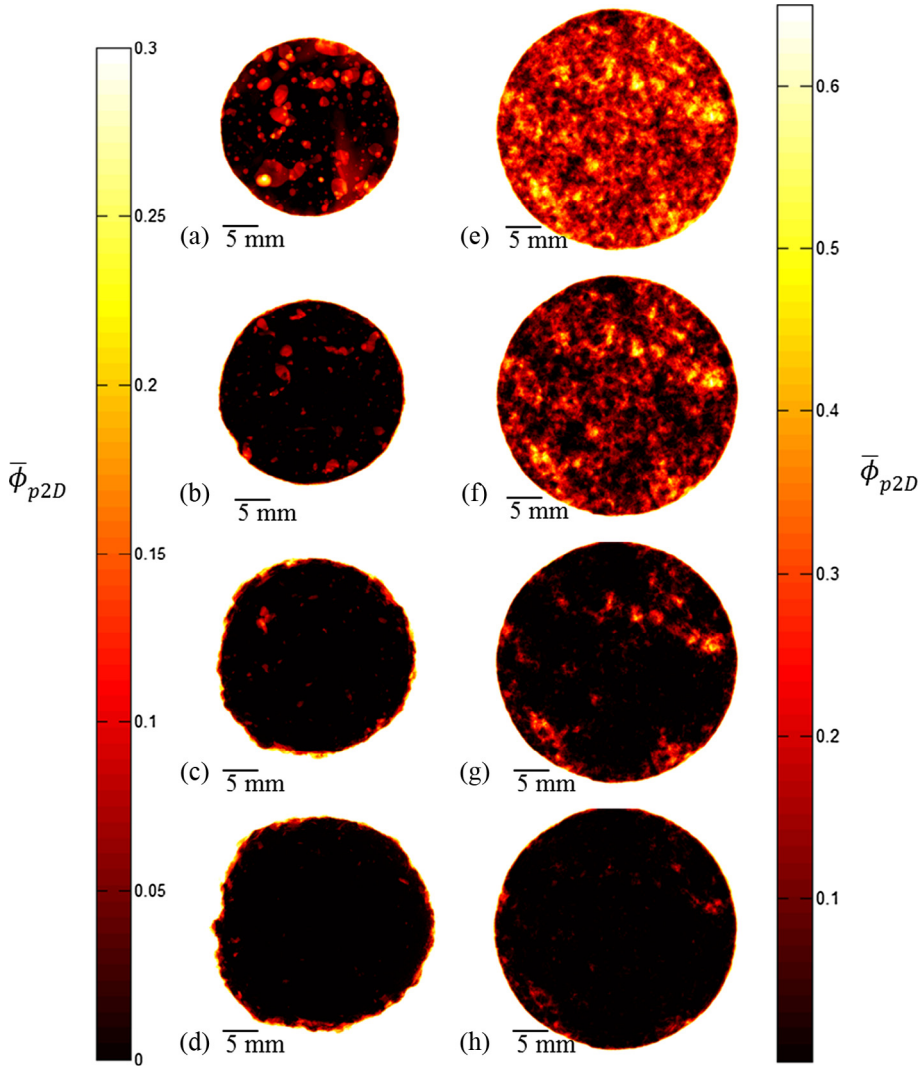

Fig. 3. 2D maps showing the porosity averaged along the thickness of samples $\overline{\phi}_{p2D}$ at various compressive strains $|\varepsilon_{33}|$: (a) 0, (b) 0.14, (c) 0.3, (d) 0.5 for the sample *S*4 and (e) 0, (f) 0.09, (g) 0.22, (h) 0.26 for the sample *H*1. (For interpretation of the references to colour in this figure legend, the reader is referred to the web version of this article.)

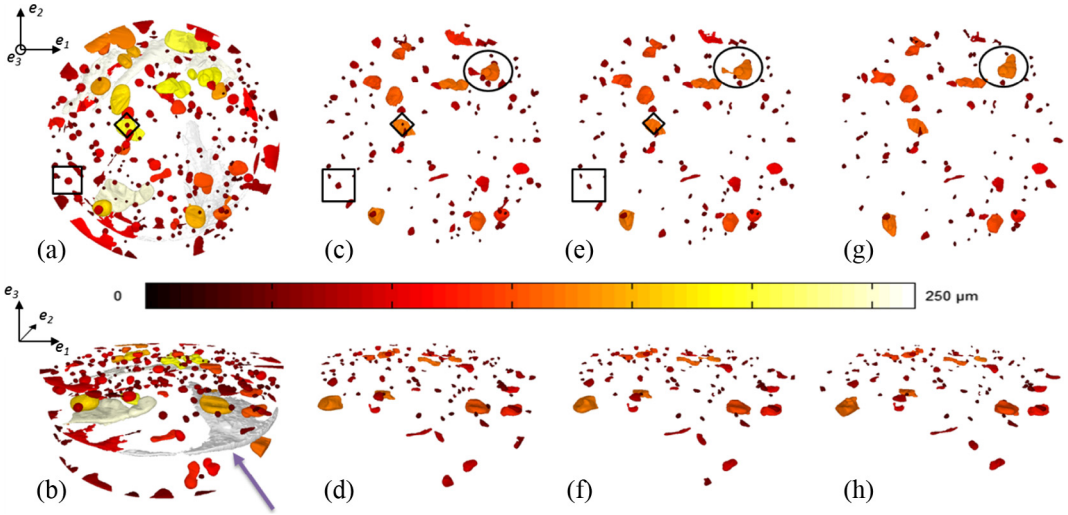

Fig. 4. 3D views showing the evolution of pores at various compressive strains $|\varepsilon_{33}|$: (a-b) 0, (c-d) 0.11, (e-f) 0.14, (g-h) 0.17 for the *S*4 sample. The equivalent diameter of the pores is colour-coded. The arrow points to an open pore between two SMC layers. The open diamond, square and circle put in the upper views illustrate pores that either disappeared or were expelled from the sample or coalesced, respectively. (For interpretation of the references to colour in this figure legend, the reader is referred to the web version of this article.)

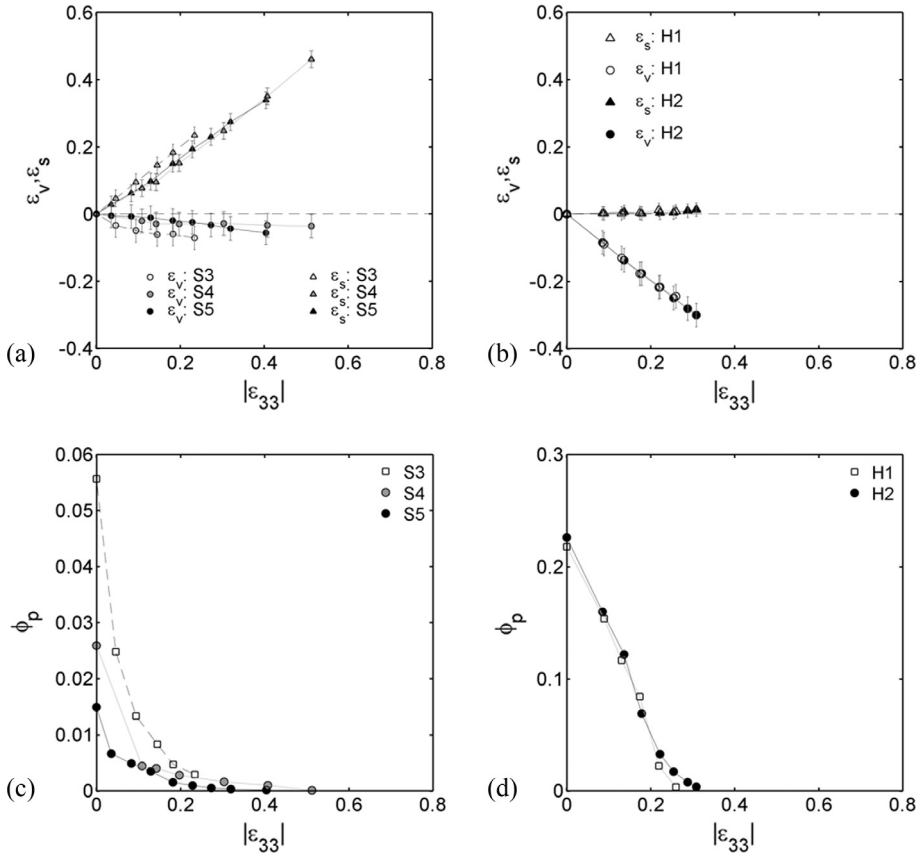

Fig. 5. Evolution of the volumetric ε_V and surface ε_S strains as a function of the axial compressive strain for the *S* (c) and *H* (d) samples. Evolution of the porosity ϕ_p as a function of the compressive strain $|\varepsilon_{33}|$ for the *S* (a) and *H* (b) samples.

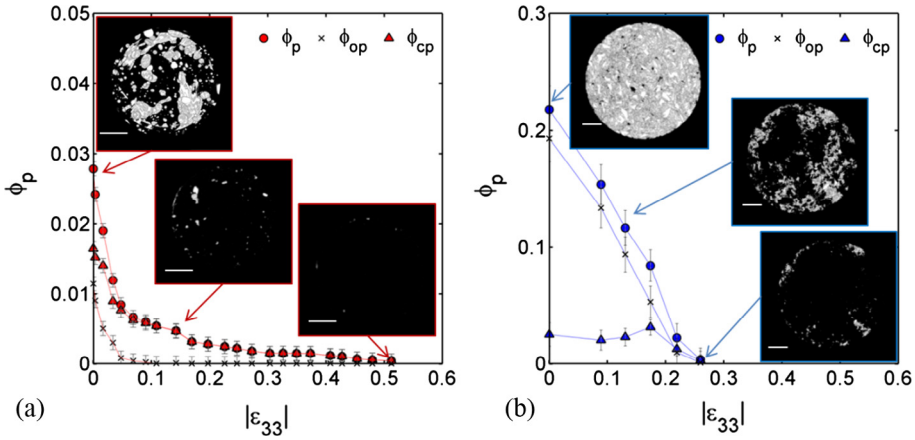

Fig. 6. Evolution of ϕ_p, ϕ_{op} and ϕ_{cp} as a function of the compressive strain $|\varepsilon_{33}|$ for the *S*4 (a) and *H*1 (b) samples. The inset correspond to the 3D upper views of the entire porous phase. The scale bar represents 5 mm. (For interpretation of the references to colour in this figure legend, the reader is referred to the web version of this article.)

Their potential origin could be the gases entrapped between the stacked layers of the specimen.

In contrast, both the morphology and the content of the initial pore phase of the *H* formulation were completely different (Figs. 2 (b) and 3(e)). The initial porosity was much higher than that of the *S* formulation, *i.e.*, $\phi_{p0} \approx 0.23$ (Fig. 5(b)), and most of pores were open since $\phi_{cp0} \approx 0.02$ (Fig. 6(b)). Fig. 2(b) shows that the matrix mainly impregnated the fibre bundles. It also formed mesoscale menisci at the vicinity of contact zones between fibre bundles, leading to complex morphologies of the porous phase, with networks made of connected and flat pores with intricate shapes.

3.2. Flow-induced strains and pores

3.2.1. Macroscale strains and porosity

During compression, the *S* samples flowed in the sheet plane (Fig. 3(a)–(d)). The flow was accompanied by a progressive and limited consolidation which tended to stabilise at high compressive

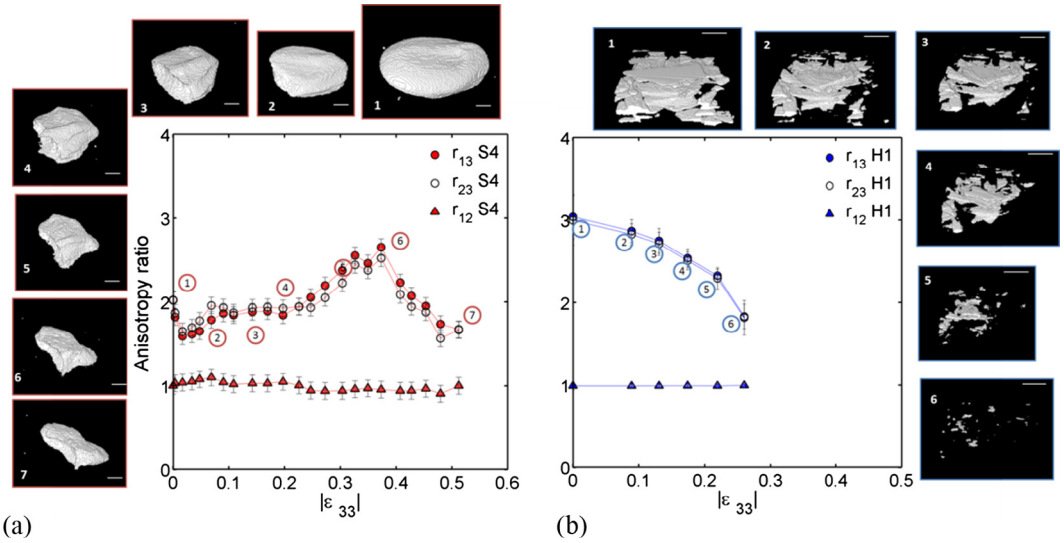

Fig. 7. Evolution of the anisotropic ratios r_{12}, r_{23}, r_{13} as a function of the compressive strain $|\varepsilon_{33}|$ for the *S*4 (a) and *H*1 (b) samples. The inset images represent the typical shape evolution of the pores. Scale bars correspond to 1 mm. (For interpretation of the references to colour in this figure legend, the reader is referred to the web version of this article.)

strains (Fig. 5(c)). This volume strain, *i.e.*, $\varepsilon_V \approx -0.02/-0.06$, exhibited a small magnitude compared with the value of -0.5 reached by the compressive strain ε_{33} and was accompanied by a decrease in the sample porosity (Fig. 5(a) and insets in Fig. 6(a)). Also note that samples *S*4 and *S*5, which had almost the same initial porosity ϕ_{p0}, also exhibited similar evolutions of their surface and volumetric strains (Fig. 5(c)), showing that the strain rate and its history had minor effects on these kinematic variables.

The compressions of the two *H* specimens were very different. Indeed, during the experiments, no in-plane flow was observed up to the 2-kN force that the micro-rheometer enabled (Fig. 3 (e)–(h)) and the surface strain ε_S remained close to 0 (Fig. 5(d)). Instead, noteworthy consolidation occurred as the sample volumetric strain ε_V decreased down to -0.25, thus leading to a progressive decrease of the sample porosity (Fig. 5(b) and inset in Fig. 6(b)). Fig. 5(b) and (d) clearly show that the consolidation mechanisms of the *H* specimens were not affected by the strain rate: surface strain, volumetric strain as well as the specimen porosity were nearly identical although these samples were deformed at two different initial compressive strain rates (Table 1).

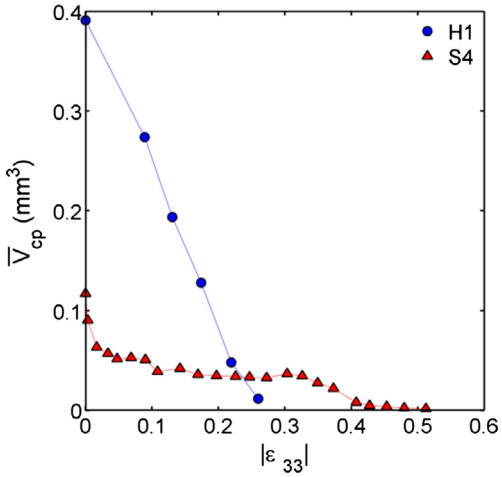

Fig. 8. Evolution of the mean closed pore size $\overline{V}_{cp}$ as a function of the compressive strain $|\varepsilon_{33}|$ for the *S*4 and *H*1 samples. (For interpretation of the references to colour in this figure legend, the reader is referred to the web version of this article.)

3.2.2. Overall pore morphology

Fig. 6(a) shows that the open pores of the *S* formulation practically disappeared in the early stages of the compression, *i.e.*, for $|\varepsilon_{33}| < 0.05$. Fig. 4(b) and (d) shows that the related mechanisms corresponded to the closure of the thin space between stacked layers. Above this value, only closed pores remained in the sample and progressively disappeared while the compressive strain decreased. During this process, the mean pore volume $\overline{V}_{cp}$ also gradually decreased (Fig. 8). At the same time, the transverse isotropy of pores exhibited a complex evolution (Fig. 7(a)). It firstly increased (from point ② to point ⑥) and then decreased (from point ⑥ to point ⑦).

During compression, the pore morphology of the *H* formulation evolved in a different way. Open porosity ϕ_{op} remained in the samples up to very high values of $|\varepsilon_{33}|$ and followed the trend observed for the total porosity (Fig. 6(b)). In parallel, the closed porosity ϕ_{cp} remained constant up to high values of $|\varepsilon_{33}|$ and then decreased. Finally closed pores disappeared in the last stages of the tests (Fig. 6(b)). At the same time, the mean volume of closed pores $\overline{V}_{cp}$ showed a sharp and constant decrease (Fig. 8). Combined with the two previous remarks, this demonstrates that during compression open pores progressively disappeared while an increasing number of smaller and smaller closed pores were forming. Lastly, it is also interesting to note that the initial transverse isotropy of the porous phase progressively decreased and tended to be isotropic (graph and micrograph in Fig. 7(b)).

3.2.3. Pore scale flow mechanisms

The 3D images in Fig. 4 and the surrounding 3D views in Fig. 7 reveal that the aforementioned trends were induced by more complicated pore scale mechanisms. For instance, the transverse isotropy that both formulations exhibited resulted in averaging the complex shape of pores due to their flow/motion and compression through the network of fibre bundles. For example, Fig. 7 shows that the considered closed pore which had an initial rounded transversely ellipsoidal shape was progressively stretched, confined and sheared. It progressively gained a complicated anisotropic shape during compression. In addition, the porosity decrease shown in Figs. 5(a) and (b) and 6 resulted from various mechanisms that were identified thanks to a close inspection of the 3D images in

Fig. 4. For example, during compression, closed pores exhibited compaction but also 3D motions with, in the case of the *S* formulation, noticeable in-plane flow which led some pores (i) to coalesce and/or (ii) to be expelled from the compressed samples, mainly through their lateral surfaces (Fig. 4(a), (c), (e), (g)).

4. Discussion

It is worth recalling that the observations carried out in this study, as well as the following discussion, are limited to objects or heterogeneities with a size that remains above the spatial resolution of the 3D images, *i.e.*, above approximately twice the voxel size (23^3 μm^3). Keeping this important point in mind, the aforementioned results show that combining compression tests with 3D images enabled the compressibility of SMCs and their related pore scale mechanisms to be suitably characterised.

4.1. Origins of pores

As already reported in previous studies [4–6], our observations confirm that prepregs such as SMCs usually exhibit pores after their fabrication. Pores in SMCs can be induced during the polymer paste preparation and mixing, the paste impregnation through the network of fibre bundles *via* calendering operations, and the ageing/maturation stage of the produced sheets before compression moulding. In this study, it was additionally shown that both the content and the morphology of pores depended on the volume fraction of fibres: the higher the volume fraction of fibres, the higher the initial volume fraction of pores and the more connected the porous phase. Two major reasons could explain this trend. First, as for other porous media, increasing the fibre content in fibrous networks usually leads to reducing their permeability [43,44]. Thus, this phenomenon could limit the impregnation of SMCs by the polymer paste [45]. Unfortunately, due to the low contrast between the matrix and the fibre bundles, we could not estimate the permeability tensor of the fibrous phase for the *H* samples (Fig. 2(b)). Thus, it was not possible to compare it to that of the *S* samples. Possible solutions to circumvent these effects would consist in either lowering the paste viscosity during the impregnation, *e.g.* by increasing its temperature, or modifying the surface properties of the fibre bundles (sizing) or the matrix to optimise the wetting of the fibrous network by the matrix. The second important reason is related to the fibre content in the prepregs. Increasing the fibre content by compacting the fibrous networks, *e.g.* during the calendering of SMCs, is known to increase their elastic energy [46,47]. Hence, the elastic energy stored during the calendering could be at the origin of springback effects, *i.e.*, deconsolidation of the fibrous networks and consequently nucleation of pores in SMCs. The higher the fibre content after the calendering phase, and the higher the stored elastic energy, the springback effects, and the pore contents before compression. Finally, the 3D images also revealed the presence before compression of a significant amount of pores between SMC layers (arrow in Fig. 4). This type of porosity was mainly induced by the wavy surfaces of prepregs that were induced by the crenelated shapes of calendering rolls [1,6]. It was shown that this type of porosity mainly disappeared in the early stages of compression, but some residual pores remained during compression. A possible solution to minimise them would consist of a last calendering operation using flat rolls.

4.2. Compressibility of SMCs

In accordance with the trends that have already been reported in previous studies [8], it was shown that the initial porosity of SMCs systematically resulted in macroscale compressible flows of SMC specimens during compression, regardless of the fibre content. The magnitude of the SMC compressibility depended on the initial pore content and was very high for the high fibre content *H* formulation. In addition, the experimental data suggested that macroscale and mesoscale compressibility mechanisms could be considered to be independent of the strain rate. Finally, depending on the type of pores, *i.e.*, closed *vs.* connected pores, the experimental results also showed that the SMC flow was different (see also the next subsection). As mentioned in the introduction, the compressibility is not taken into account in rheological models for prepregs such as SMCs (or GMTs) or other similar unsaturated concentrated fibre suspensions to the best of our knowledge, although it was shown in this study that compressibility could drastically alter the flow of these materials (Fig. 5(c) and (d)). Thus, these results constitute an interesting database linking macroscale flow phenomena to pore scale compressibility mechanisms that can be used to build relevant constitutive theories which could be implemented in simulation software for compression moulding processes.

4.3. Related mesoscale flow mechanisms

Two types of flow mechanisms were identified and correlated with the types of pores in SMCs, namely open or closed pores.

4.3.1. Open pores

The first flow mode mainly occurred for tests performed with the *H* specimens, at least up to compressive strains $|\varepsilon_{33}|$ below 0.2. It was also observed to a less extent during the first compression stages of the *S* specimens, *i.e.*, for compressive strains $|\varepsilon_{33}|$ below 0.05. In these situations, the main SMC flow mode was transverse consolidation with pronounced compressibility effects. Since the studied SMCs contained a sufficient amount of connected pores (Fig. 6(a)), the permeability of the porous phase was large enough so that air/gases in pores could be expelled from the SMCs during compression, leading to a progressive closure of pores. However, during compression, the extraction of air/gases from the open pores possibly became more and more difficult and complex flow mechanisms took place. This is illustrated in Fig. 9 that shows the evolution of the diagonal components of the permeability tensor **K** of the porous phase for the *H* samples during compression (the non-diagonal components were negligible and were thus

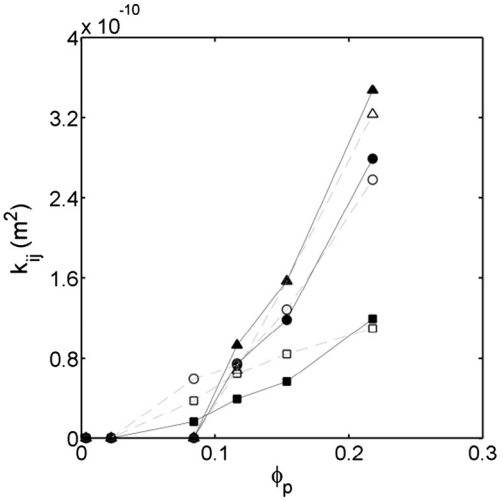

Fig. 9. Evolution of the components k_{11}(*circles*), k_{22}(*triangles*), k_{33}(*square*) of the pore phase permeability tensor **K** as a function of the pore content ϕ_p for the two tested *H* samples (black and with marks).

omitted for clarity). The permeability components underlined once again the transverse isotropy of pores (the out-of-plane permeability component being different from the in-plane ones) and exhibited a sharp decrease during compression, but were not zero up to the two last compression stages. It is also interesting to note that during the first stages of compression, the flow in pores should rather occur in the sheet plane as the in-plane permeability components were higher than the out-of-plane components (Fig. 9). This scenario should be reversed at the end of compression (Fig. 9). From a practical standpoint, these results are be interesting in order to optimise vacuum assisted compression mouldings, *e.g.* by optimising the placement and the activation of the void extractors.

4.3.2. Closed pores

The second flow mechanism occurred when the SMCs, such as the *S* formulation, principally contained closed pores. In this case, the compressibility and the related consolidation mechanisms of SMCs were much weaker than those obtained for the first flow mode, leading to substantial in-plane flow, *i.e.*, perpendicular to the compression axis $\mathbf{e}_3$. Closed pores exhibited complex kinetics and kinematics with coalescence, shrinkage up to full closure (see next paragraph) and motion up to the external surfaces of the samples, as shown qualitatively in Fig. 4.

To better understand these intricate mechanisms, Fig. 10(a) shows the deviation Δx_{G_i} of the pore placement $\tilde{\mathbf{x}}_{G_i}^{exp}$ with respect to the affine prediction $\tilde{\mathbf{x}}_{G_i}^{aff}$: obviously, Δx_{G_i} reached very high values. In addition, as emphasised in Fig. 10(b), the in-plane trajectories $\tilde{\mathbf{x}}_{G_i}^{exp}$ and $\tilde{\mathbf{x}}_{G_i}^{aff}$ exhibited two major differences: (i) the experimental in-plane velocities of closed pores were much faster than those predicted by the affine assumption, and (ii) most of the experimental trajectories exhibited noticeable angular deviations from the affine radial trajectories. The first difference is similar to that observed during the transport of bubbles in capillaries [48,49], where bubbles are prone to flow faster than their suspending fluid, due to shear stress and pressure gradient effects and to related bubble deformation mechanisms. Westerberg et al. [50] also reported the same trend by squeezing between two parallel platens grease with air bubbles which exhibited radial velocities faster than the squeezed grease. In the present lubricated compression experiments, the phenomena were similar but much more complex due the presence of fibre bundles: our results suggest that closed pores were transported in tortuous capillaries induced by the fibrous networks.

It is also interesting to notice that closed pores were also subjected to severe shrinkage and sometimes disappeared (Figs. 4 and 8). This shrinkage was linked with the pore pressure p_p that was estimated according to the following procedure. We first estimated the macroscale compression stress $\sigma_{33} = F/\overline{A}$ recorded during the experiments, F and $\overline{A}$ being the compression force and the macroscale in-plane surface of the samples, respectively. Then, the following assumptions were stated: (i) the surface tension effects at the pore-SMC interfaces were negligible because of the very high shear viscosity of SMCs (≈10000 Pa s), (ii) dense SMCs (without pores) behaved as incompressible materials, (iii) and the SMC extra-stress tensor was purely deviatoric (rigorously, this assumption may be questionable taking into account the high anisotropy of SMCs [29], but was expected to provide a good order of magnitude). Hence, when open pores disappeared, *i.e.*, for $\varepsilon_{33} < -0.05$ for the specimen *S*4 (Table 1), the mean pressure $\overline{p}_p$ in closed pores of mean volume $\overline{V}_{cp}$ was estimated as $\overline{p}_p \approx p_a - \sigma_{33}/3$, where p_a was the atmospheric pressure.

The resulting evolution of $\overline{p}_p$ during the compression of the specimen *S*4 is shown in Fig. 11 as a function of $\overline{V}_{cp}$ for $\varepsilon_{33} < -0.05$: only a small increase in the pore pressure $\overline{p}_p$ occurred during compression, *i.e.*, from 0.15 to 0.17 MPa. In parallel, another estimate $\overline{p}_p^{igl}$ of the closed pore pressure was provided using the values of $\overline{p}_p$ and $\overline{V}_p$ for $\varepsilon_{33} = -0.1$ for the considered sample, and the mean number of moles $\overline{n}$ of gases (probably a mixture of air and styrene) contained in the pores and calculated from the ideal gas law (*igl*). Then, assuming that $\overline{n}$ remained constant during compression, *i.e.*, there was no molecule adsorption/diffusion at the interface between the pores and SMC, $\overline{p}_p^{igl}$ was computed both from the ideal gas law and the evolution of $\overline{V}_{cp}$ plotted in Fig. 8. Obviously, Fig. 11 shows that $\overline{p}_p$ and $\overline{p}_p^{igl}$ exhibited completely different evolution so that $\overline{p}_p^{igl}$ was one hundred times higher than $\overline{p}_p$ at the end of the compression. Consequently, this result tends to prove that approximately 99% of the gas molecules initially inside closed pores disappeared during the compression-induced pore shrinkage, most of them being probably dissolved in the SMC matrix. Note that rather similar phenomena have been reported by Leterrier and G'Sell [22] for the dissolution of gases during the compression of glass-reinforced thermoplastic composites.

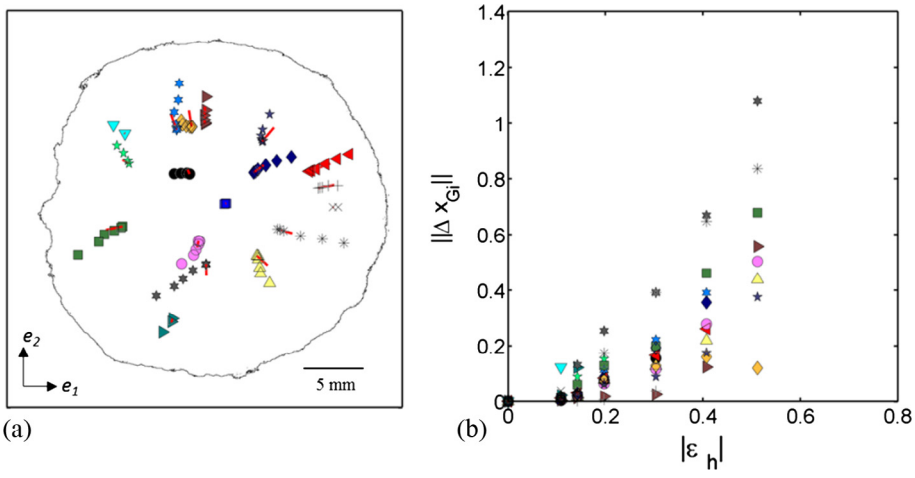

Fig. 10. (a) In-plane motion of the centres of mass of several closed pores manually identified during the compression of the sample *S*4 (from Fig. 3) and compared to the affine motion given by Eq. (2). (b) Related deviation Δx_{G_i} as a function of the compressive strain $|\varepsilon_{33}|$. (For interpretation of the references to colour in this figure legend, the reader is referred to the web version of this article.)

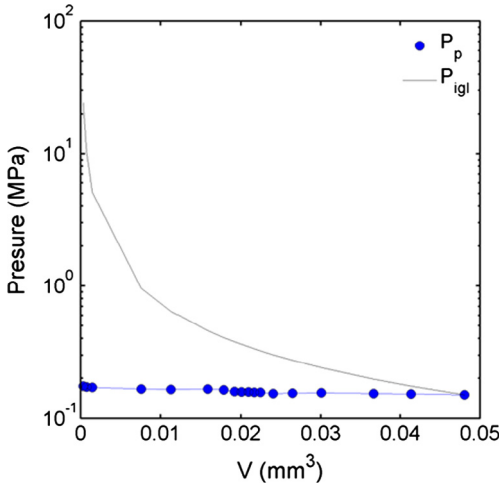

Fig. 11. Evolution of the estimated mean pore pressures $\overline{p}_p$ and $\overline{p}_p^{igl}$ as a function of the mean volume of pores $\overline{V}_{cp}$ for the sample *S*4. (For interpretation of the references to colour in this figure legend, the reader is referred to the web version of this article.)

5. Conclusion

The compressibility and the porosity of two SMCs having high and moderate fibre contents, respectively, were investigated using synchrotron X-ray microtomography. This technique enabled a better understanding of the mechanisms that are related to the macroscale flow as well as the kinetics and the kinematics of pores in these prepregs during their compression. Thus, for the first time, *in situ* and 3D images of the flow of several SMC samples as well as their evolving porous mesostructures were acquired. In the initial state, SMC samples were generally porous and contained transversely isotropic pores. The volume fraction and the morphology of the pores depended on the fibre content. The porosity was elevated and the pores were mainly open at high fibre content. On the contrary, at moderate fibre content, the porosity was moderate and the pores were mainly closed. Optimising the sizing of the fibre bundles to improve their wetting properties, together with minimising the elastic energy stored in the fibrous reinforcement during the calendering phase could provide two proper solutions to minimise the SMC initial porosity. In addition, this study showed that the compressibility of both studied SMCs was associated with a decrease in the sample porosity, both being practically independent of the strain rate. As these phenomena could be particularly important for high fibre content SMC formulations, they should be taken into account in future rheological models for the numerical simulation of the compression moulding process. Finally, the 3D *in situ* images also provided useful information to better understand pore compressibility and transport mechanisms. The first primary mechanisms occurred for connected pores, *i.e.*, mainly for high fibre content SMC. During compression, these pores reduced in size and, simultaneously, the gases that they contained could flow through the open pore network and be expelled from the samples. The second mechanisms were related to closed pores and were mainly observed for moderate fibre contents. During compression, closed pores decreased in size and sometimes coalesced. Combining the 3D images and the compression stress recorded during the experiments, it was shown that the pore shrinkage was related to the dissolution of pore gases (air, styrene) into the SMC polymer paste. Besides, these closed pores were also expelled from the centre of samples to the sample external surfaces, following tortuous trajectories and exhibiting displacements that were faster than that of the bulk SMC flow. This phenomenon was attributed to the squeezing effect exerted by the complex fibre bundle network on the SMC paste and the closed pores. The proper modelling of these complex mechanisms would require further investigation of other representative mechanical loadings, *e.g.* plane strain compression, tensile or shear loadings, and higher testing temperatures.

References

[1] Orgéas L, Dumont PJJ. The Wiley Encyclopedia of Composites. 2nd ed. Wiley; 2012. p. 2683–718. Ch. Sheet Molding Compounds.
[2] Silva-Nieto RJ, Fisher BC. Rheological characterization of unsatured polyester resin sheet molding compound. Polym Eng Sci 1981;21(8):499–506.
[3] Lee CC, Folgar F, Tucker CL. Simulation of compression molding for fiber-reinforced thermosetting polymers. J Eng Ind 1984;106:114–25.
[4] Comte E, Mehri D, Michaud V, Månson J-AE. Void formation and transport during SMC manufacturing: effect of the glass fiber sizing. Polym Compos 2006;27:289–98.
[5] Le TH, Dumont PJJ, Orgéas L, Favier D, Salvo L, Boller E. X-ray phase contrast microtomography for the analysis of the fibrous microstructure of SMC composites. Compos Part A-Appl Sci Manuf 2008;39:91–103.
[6] Guiraud O, Dumont PJJ, Orgéas L. How to prepare SMC and BMC-like compounds to perform relevant rheological experiments? Appl Compos Mater 2013;20:157–69.
[7] Caba AC, Loos AC, Batra RAC. Fiber-fiber interaction in carbon mat thermoplastics. Compos Part A-Appl Sci Manuf 2007;38:469–83.
[8] Guiraud O, Dumont PJJ, Orgéas L, Favier D. Rheometry of compression moulded fibre-reinforced polymer composites: rheology, compressibility, and friction forces with mould surfaces. Compos Part A-Appl Sci Manuf 2012;43:2107–9.
[9] Odenberger PT, Andersson HM, Lundström TS. Experimental flow-front visualisation in compression moulding of SMC. Compos Part A-Appl Sci Manuf 2004;35:1125–34.
[10] Waas AM, Schultheisz CR. Compressive failure of composites, Part II: Experimental studies. Prog Aerospace Sci 1996;32:43–78.
[11] Naidu MS, Kamaraju V. High voltage engineering. New York, USA: McGraw-Hill; 1996.
[12] Yamada H, Mihata I, Tomiyama T, et al. Investigation of the fundamental causes of pinholes in SMC moldings. In: Proc. of 47th annual conference, composites institute, the society of the plastics industry Inc, Cincinnati, Ohio, USA..
[13] Olsson NEJ, Lundström TS, Olofsson K. Design of experiment study of compression moulding of SMC. Plast, Rubber Compos 2009;38:426–31.
[14] Evans A, Qian C, Turner T, Harper L, Warrior N. Flow characteristics of carbon fibre moulding compounds. Compos Part A-Appl Sci Manuf 2016;90:1–12.
[15] Barone MR, Caulk DA. A model for the flow of a chopped fiber reinforced polymer compound in compression molding. J Appl Mech 1986;53 (191):361–70.
[16] Osswald TA, Tucker CL. Compression mold filling simulation for non-planar parts. Int Polym Process 1990;5:79–87.
[17] Abrams LM, Castro JM. Predicting molding forces during Sheet Molding Compound (SMC) compression molding. I: Model development. Polym Compos 2003;24:291–303.
[18] Dumont P, Orgéas L, Favier D, Pizette P, Venet C. Compression moulding of SMC: in situ experiments, modelling and simulation. Compos Part A-Appl Sci Manuf 2007;38:353–68.
[19] Marjavaara BD, Ebermark S, Lundström TS. Compression moulding simulations of SMC using a multiobjective surrogate-based inverse modelling approach. Mech Compos Mater 2009;45:503.
[20] Kluge NEJ, Lundström TS, Westerberg LG, Olofsson K. Compression moulding of sheet moulding compound: modelling with computational fluid dynamics and validation. J Reinf Plast Compos 2015;34:479–92.
[21] Kardos JL, Dudukovic MP, Dave R. Void growth and resin transport during processing of thermosetting – matrix composites. Adv Polym Sci 1986;80:101–23.
[22] Leterrier Y, G'Sell C. Formation and elimination of voids during the processing of thermoplastic matrix composites. Polym Compos 1994;15:101–5.
[23] Centea T, Hubert P. Measuring the impregnation of an out-of-autoclave prepreg by micro-CT. Compos Sci Technol 2011;71:593–9.
[24] Helmus R, Kratz J, Potter K, Hubert P, Hinterhölzl R. An experimental technique to characterize interply void formation in unidirectional prepregs. J Compos Mater 2016. http://dx.doi.org/10.1177/0021998316650273.
[25] Maire E, Buffières J-Y, Salvo L, Blandin J-J, Ludwig W, Létang J-M. On the application of X-ray microtomography in the field of material science. Adv Eng Mater 2001;3:539–46.
[26] Limodin N, Salvo L, Boller E, Suéry M, Felberbaum M, Gailliegue S, et al. In situ and real-time 3-D microtomography investigation of dendritic solidification in an Al–10 wt.% Cu alloy. Acta Mater 2009;57:2300–10.
[27] Laurencin T, Orgéas L, Dumont PJJ, Rolland du Roscoat S, Laure P, Le Corre S, et al. 3D real-time and in situ characterisation of fibre kinematics in dilute non-newtonian fibre suspensions during confined and lubricated compression flow. Compos Sci Technol 2016;134:258–66.
[28] Le Corre S, Orgéas L, Favier D, Tourabi A, Maazouz A, Venet C. Shear and compression behaviour of sheet molding compounds. Compos Sci Technol 2002;62(4):571–7.

[29] Dumont P, Orgéas L, Le Corre S, Favier D. Anisotropic viscous behaviour of Sheet Molding Compounds (SMC) during compression molding. Int J Plast 2003;19(4):625–46.
[30] Guiraud O, Dumont PJJ, Orgéas L, Vassal J-P, Le TH, Favier D. Towards the mould filling simulation of polymer composites reinforced with mineral fillers and short glass fibres. Int J Mater Forming 2010;3:1313–26.
[31] Rolland du Roscoat S, Decain M, Thibault X, Geindreau C, Bloch J-F. Estimation of microstructural properties from synchrotron X-ray microtomography and determination of the REV in paper materials. Acta Mater 2007;55:2841–50.
[32] Barone MR, Caulk DA. The effect of deformation and thermoset cure on heat conduction in a chopped-fiber reinforced polyester during compression molding. Int J Heat Mass Transfer 1979;22(7):1021–31.
[33] Barone MR, Caulk DA. Kinematics of flow in sheet molding compound. Polym Compos 1985;6(2):105–9.
[34] Latil P, Orgéas L, Geindreau C, Dumont PJJ, Rolland du Roscoat S. Towards the 3D in situ characterisation of deformation micro-mechanisms within a compressed bundle of fibres. Compos Sci Technol 2011;71:480–8.
[35] Martoïa F, Cochereau T, Dumont PJJ, Orgéas L, Terrien M, Belgacem MN. Cellulose nanofibril foams: links between ice-templating conditions, microstructures and mechanical properties. Mater Des 2016;104:376–91.
[36] Paganin D, Mayo SC, Gureyev TE, Miller PR, Wilkins SW. Simultaneous phase and amplitude extraction from a single defocused image of an homogeneous object. J Microsc 2002;206:33–40.
[37] Schindelin J, Arganda-Carreras I, Frise E, Kaynig V, Longair M, Pietzsch T, et al. Fiji: an open-source platform for biological-image analysis. Nat Methods 2012;9:676–82.
[38] Doube M, Klosowski MM, Arganda-Carreras I, Cordelières F, Dougherty RP, et al. Bonej: Free and extensible bone image analysis in imagej. Bone 2010;47:1076–9.
[39] Underwood EE. Quantitative Stereology. Menlo Park, California – London – Don Mils, Ontario, USA: Addison-Wesley Publishing Company; 1970.
[40] Auriault J-L, Boutin C, Geindreau C. Homogenization of coupled phenomena in heterogenous media. ISTE and Wiley; 2009.
[41] Rolland du Roscoat S, Decain M, Geindreau C, Thibault X, Bloch J-F. Microstructural analysis of paper using synchrotron X-ray microtomography: numerical estimation of the permeability and effective thermal conductivity. Appita J 2008;61:286–90.
[42] Chalencon F, Dumont PJJ, Orgéas L, Foray G, Cavaillé J-Y, Maire E. Homogeneous and heterogeneous rheology and flow-induced microstructures of a fresh fiber-reinforced mortar. Cem Concr Res 2016;82:130–41.
[43] Jackson GW, James DF. The permeability of fibrous porous media. Can J Chem Eng 1986;64:364–74.
[44] Comas-Cardona S, Binétruy C, Krawczak P. Unidirectional compression of fibre reinforcements. Part 2: A continuous permeability tensor measurement. Compos Sci Technol 2007;67:638–45.
[45] Michaud V, Mortensen A. Infiltration processing of fibre reinforced composites: governing phenomena. Compos Part A-Appl Sci Manuf 2001;32:981–96.
[46] Toll S. Packing mechanics of fiber reinforcements. Polym Eng Sci 1998;38:1337–50.
[47] Comas-Cardona S, Le Grognec P, Binetruy C, Krawczak P. Unidirectional compression of fibre reinforcements. Part 1: A non-linear elastic-plastic behaviour. Compos Sci Technol 2007;67:507–14.
[48] Fairbrother F, Stubbs AE. Studies in electroendomosis part IV. The bubble-tube method of measurements. J Chem Soc 1935;1:527–9.
[49] Bretherton FP. The motion of long bubbles in tubes. J Fluid Mech 1961;10:166–88.
[50] Westerberg LG, Olsson NEJ, Lundström TS. Transport of bubbles during compression in a non-Newtonian fluid. In: Proc. of ITP2009: interdisciplinary transport phenomena VI: fluid, thermal, biological, materials and space sciences. Volterra, Italy.